Research Paper

Validation of precipitable water vapor estimates from an inexpensive infrared thermometer

Alejandro Jesús Pérez Aparicio [a,b,c], Javier Vaquero-Martínez [d,b], María Cruz Gallego [a,b], Manuel Antón [a,b], José Manuel Vaquero [a,b,*]

[a] Departamento de Física, Universidad de Extremadura, 06006, Badajoz, Spain
[b] Instituto Universitario de Investigación del Agua, Cambio Climático y Sostenibilidad (IACYS), Universidad de Extremadura, 06006, Badajoz, Spain
[c] Earth Remote Sensing Laboratory (EaRSLab) and Institute of Earth Sciences – ICT (Polo de Évora), Instituto de Investigação e Formação Avançada (IIFA), Universidade de Évora, 7000-671, Évora, Portugal
[d] Departamento de Didáctica de las Ciencias Experimentales y las Matemáticas, 10071, Cáceres, Spain

ARTICLE INFO

ABSTRACT

Water vapor is a fundamental component of the Earth's atmosphere with a high spatial and temporal variability. This work studies to what extent low-cost infrared thermometers can infer precipitable water (variable commonly used to characterize atmospheric water vapor). In a calibration process, infrared thermometer readings recorded at Badajoz (Spain) during the 2015–2018 period are compared against precipitable water data measured with reference ground-based Global Navigation Satellite Systems (GNSS) in order to obtain conversion factors through regression analyses considering two exponential fits. After this calibration, using the equation of the best fit, thermometer readings for the year 2019 are transformed into precipitable water estimates. A validation analysis in which these estimates are compared with GNSS measurements yields rms differences of 19% and 17% when normal and seasonal calibration had been employed, respectively. These results are similar (or even better) to those obtained with satellite data. In addition, we explore if certain factors, such as solar elevation, precipitable water content, precipitable water measurements used as reference and equations to convert temperature readings into precipitable water estimates, can significantly affect the quality of the estimates. In view of our results, low-cost infrared thermometers could be used to create an extensive and dense network for a better characterization of the spatial and temporal variability of water vapor.

1. Introduction

Water vapor is a trace gas of the atmosphere with a fundamental role in the climate system. It is the main absorbent of infrared radiation from the Earth's surface, which makes it responsible for the heating of low layers of air. Moreover, water vapor latent heat constitutes a very efficient mechanism for energy transport: water is evaporated at low latitude regions, and then, it is transported to high latitudes, where it condenses, releasing high amounts of heat (Myhre et al., 2013). Water vapor is the most important natural greenhouse gas, and it is considered to generate a positive feedback in the climate system, according to general circulation models (Colman, 2003, 2015).

Water vapor data can refer to different variables, like the relative or absolute humidity at certain height (or the whole profile), concentration, mixing ratio, and so on. In this work, we focus on the precipitable water (PW), also known by other names, like precipitable water vapor, total column water vapor or integrated water vapor. PW is equivalent to the height that all water vapor in a vertical cylinder of unit cross section would reach in a vessel of the same cross section if it precipitated. Therefore, it is commonly expressed in length units (mm or cm). It must be noticed that this height corresponds to units of superficial density if liquid water density (~ 1 g cm^{-3}) is considered (kg m^{-2} or g cm^{-2}, respectively).

Due to its importance in the climate system, the scientific community is interested in obtaining quality data for water vapor. There are several kinds of instruments that can measure PW. Radiosondes are typically used as reference because of their quality and the fact that their measuring technique is direct. However, radiosounding is an expensive technique. Therefore, stations with radiosounding are relatively scarce, and measurements are taken between 1 and 4 times a day (Negusini

et al., 2021; Vaquero-Martínez et al., 2019).

Ground-based Global Navigation Satellite Systems (GNSS) can provide measurements of PW, following a technique developed by Bevis et al. (1994, 1992), with a high temporal resolution. GNSS networks are becoming more dense as they are useful to a wide range of geodetic and earth-science interests, and easy to maintain (Guerova et al., 2016; Vaquero-Martínez and Antón, 2021).

Other instruments measuring PW are based on the measurement of radiation, such as sun photometers, microwave radiometers, and so on. These instruments can measure radiation in specific absorption bands, which are sensible to PW. They generally use complex algorithms to compute the inversion of the radiative transfer equations for obtaining estimates of PW from the radiation observed (Bokoye et al., 2003; Buehler et al., 2012).

Currently, infrared thermometers are used to detect clouds for meteorological and astronomical purposes since these devices act as radiometers that respond to infrared radiation emitted by clouds (Morris et al., 2006). Atmospheric water vapor also emits infrared radiation. For that reason, Idso (1982) proposed the use of an infrared thermometer to measure water vapor pressure. Using low-cost devices, Mims III et al. (2011) compared readings of commercially available infrared thermometers pointed at the cloudless zenith sky with PW values from reference instruments, i.e., sun photometer and GNSS, and proposed the equation of the best fit together with the thermometer readings as input as a way to obtain PW estimates. However, they did not present, analyze, compare or validate PW estimates. Recently, Kelsey et al. (2022), following a similar procedure in another region of the US, also took cloudless zenith sky readings with low-cost infrared thermometers for two years and after a comparison with radiosonde PW values, they used the equation of the best fit (a two-coefficient exponential function instead of a three one as the previous authors) to compute PW estimates. Then, the estimates were compared with sun photometer PW measurements and GNSS ones.

The present work studies daily zenith sky infrared thermometer readings (T) taken under cloudless conditions with a low-cost device for a period of 5 years in Badajoz (Spain). They are compared against PW measurements recorded by GNSS (PW_G) through regression analyses. Two exponential fits to the data (two and three coefficients) are employed in order to assess differences in the results. Unlike previous studies, an independent period of common measurements thermometer-GNSS has been used to validate the PW estimates from the infrared thermometer (PW_t), and the dependences that the estimates present with some factors such as the seasonal behavior, PW content and solar zenith angle are examined.

2. Instruments and data

The device used in the present study was the commercial infrared thermometer Powerfix IAN 100042 (Fig. 1) with an approximate cost of 20 euros. The device gave measurements in degrees Celsius with one decimal point. However, according to the manufacturer, the measurement accuracy is 3%. In addition, the device has a temperature measurement range from −40 °C to 220 °C and a field of view of 14.3°. Daily measurements from the flat roof of our workplace (Physics Department of the University of Extremadura, 38.9° N, 7.0° W, 184 m above sea level) in Badajoz (Spain) were performed with it from December 2014 to March 2020. The procedure to obtain measurements consists in pointing the thermometer straight up at the zenith sky from a place in which the device does not receive direct solar radiation, such as the shadow of an object or the observer. The pointing procedure is carried out manually by an operator (always the same person). The zenith and its vicinity must be free of clouds, Sun or obstacles because we only want to measure the infrared radiation emitted by the atmospheric water vapor in the field of view of the device. Each reading of the instrument was written down together with the universal time, date and sky condition near the zenith in the field of view of the device. Note that, in contrast to

Fig. 1. Commercial infrared thermometer used in the present study.

previous works, for the present study, two readings a day were performed. The first one was taken immediately when the operator arrived at the flat roof carrying the thermometer (set 1). Then, the thermometer was left 1 h in the flat roof to adjust to the ambient climatic conditions and, after that, the second reading was taken (set 2). The usual time for readings was 9:00 UTC for the set 1 and 10:00 UTC for the set 2 so that the Sun was not too near the zenith.

It must be taken into account that the infrared thermometer is a device designed to average the surface temperature of nearby objects located in its field of view. In the present study, the thermometer is pointed at the zenith sky free of obstacles. Therefore, the readings do not represent the ambient temperature or sky temperature. Rather, they can be considered as a proxy for the downwelling infrared radiation emitted by the atmospheric water vapor.

PW_G measurements from a nearby GNSS receiver (in the same city, 2 km away and 11 m higher with respect to the thermometer observation site) recorded on the same days at practically the same time are used as reference to calibrate the infrared thermometer readings. Note that the GNSS measurements closest in time to T readings are chosen. GNSS measurements with a 5-min latency are available on http://geodesy.unr.edu/. Information about the GNSS technique to derive these PW_G data can be found in the work by Blewitt et al. (2018). In summary, the technique is based on the method described by Bevis et al. (1992). In the GNSS position processing, the zenith total delay (ZTD), which is the contribution of the lower atmosphere to the delay of the signal, is obtained as one of the unknowns together with the position and other variables. The ZTD can be separated into a hydrostatic part, dependable only on the surface pressure, and the wet delay (ZWD), which is related to the water vapor exclusively. This ZWD can be converted into PW_G through a multiplication factor that only depends on the mean temperature of the atmosphere weighted by the water vapor profile, also known as Davis temperature.

3. Methodology

First of all, we filtered our dataset of zenith sky temperature readings from the infrared thermometer (T) to keep only situations of clear sky, without clouds, haze, smoke or dust in the field of view of the device. Then, T measurements of the period 2015–2018 are compared against PW measurements taken at approximately the same time from a nearby GNSS receiver (PW_G) through a regression analysis considering an exponential fit of the form:

$$PW = b \cdot exp(T / c) \qquad (1)$$

as done by Kelsey et al. (2022). However, this fit has a problem: there

can be a systematic error in the data that is not represented in the equation. Therefore, it is suggested a slightly more sophisticated version of the form:

$$PW = a + b \cdot exp(T / c) \qquad (2)$$

following Mims et al. (2011). In both expressions, PW is in mm and T in °C. a, b and c are regression coefficients. To calculate these, a non-linear regression is performed with the R function *nlm*. This function needs a starting value of the coefficients, as it uses an iterative method to find the best fit. The starting coefficients are calculated using a linear regression of the form of Equation (1) taking logarithms in both sides of the equation with same *c*, *b* multiplied by 1.5 and *a* set to 0.

Both equations are tested and used to "calibrate" the thermometer with data of the period 2015–2018, i.e., to obtain an expression that converts T readings into PW estimates (PW_t). The calibration coefficients a, b and c are obtained for set 1, set 2, and all the measurements of both sets together. After evaluation, the equation and set with the best results are selected. In addition, a seasonal calibration is carried out, that is, the calibration coefficients are calculated season-wise and compared against the full-period calibration. For the seasonal analyses, spring comprises the months March, April and May, summer the months June, July and August, autumn the months September, October and November, and winter the months December, January and February.

Finally, we obtain PW_t estimates by substituting the values of the calibration coefficients a, b and c (calculated with data of the period 2015–2018) and measurements of T for the year 2019 in Equation (1) or Equation (2). Subsequently, a validation analysis with data of the year 2019 is carried out by comparing PW_t with PW_G using both full-period and season-wise models. Some statistics are considered: mean bias error (MBE), which is defined as the mean of the differences $PW_t - PW_G$; root mean squared differences (rms diff) which is the root mean of the squared differences; determination coefficient (r^2), which gives the fraction of the variance that is explained by the model. These statistics assesses the quality of the fits, the quality of the PW_t estimates and helps to decide whether a seasonal model is necessary or it is better to use the full-period model. Equations (3)–(5) show the definition of MBE, rms diff and r^2, respectively:

$$MBE = \frac{1}{n} \sum \left(PW_{t,i} - PW_{G,i} \right) \qquad (3)$$

$$rmsdiff = \sqrt{\frac{1}{n} \sum \left(PW_{t,i} - PW_{G,i} \right)^2} \qquad (4)$$

$$r^2 = \frac{\left(\sum \left(PW_{G,i} - \overline{PW_G} \right) \left(PW_{t,i} - \overline{PW_t} \right) \right)^2}{\sum \left(PW_{G,i} - \overline{PW_G} \right)^2 \sum \left(PW_{t,i} - \overline{PW_t} \right)^2} \qquad (5)$$

4. Results and discussion

4.1. Calibration

Fig. 2 displays scatter plots of PW_G vs T for the period January 2015–December 2018. As explained in the previous section, two datasets are shown in this plot: measurements performed immediately when the operator arrived at the flat roof (set 1 as red dots) and those performed after the thermometer have adjusted to the ambient climatic conditions after 1 h (set 2 as green triangles).

Firstly, regression analyses are carried out considering an exponential fit of two coefficients (Equation (1)) and other of three ones (Equation (2)). The coefficients a, b, c, the determination coefficient and root mean square differences are listed in Table 1 and Table 2.

Fig. 2 reveals that temperature from set 1 (T_1) is associated with

Table 1

Coefficients of the fit equation $PW_G = b \bullet exp(T/c)$, determination coefficients, rms differences and percent rms differences for 3 cases: all the measurements are considered (both sets); those taken immediately when the operator arrived at the flat roof (set 1); those taken after the thermometer have adjusted to the ambient climatic conditions (set 2).

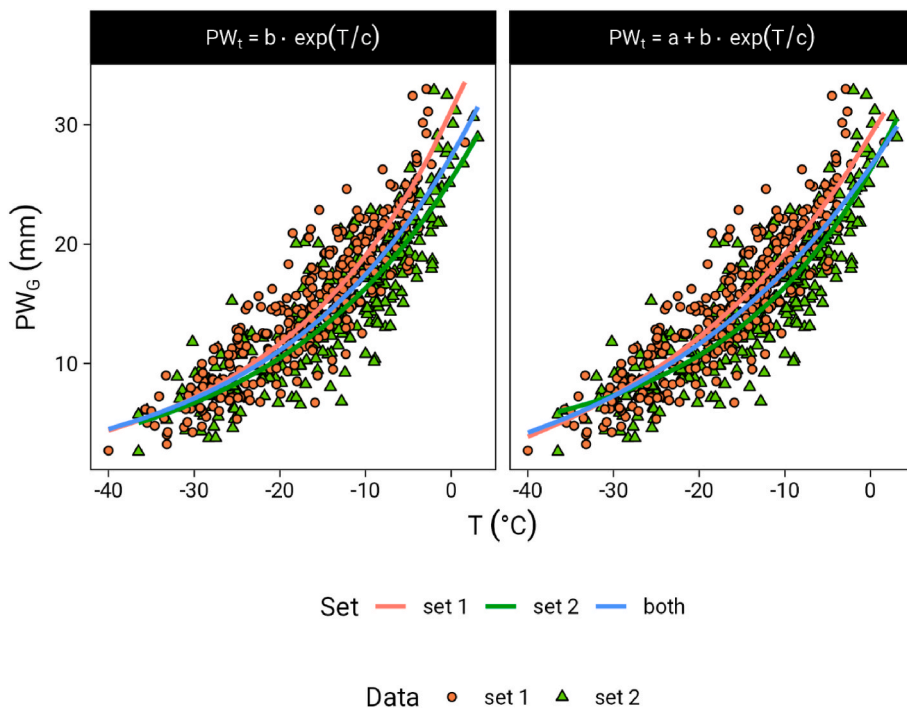|	Both sets	Set 1	Set 2
b (mm)	27.38	31.04	25.42
c (° C^{-1})	0.05	0.05	0.04
r^2	0.755	0.790	0.783
rms diff (mm)	2.98	2.72	2.84
rms diff/mean (%)	19.86	18.35	18.72

Fig. 2. Scatter plot of precipitable water measured by a nearby GNSS receiver (PW_G) vs zenith sky temperature readings performed with an infrared thermometer (T) for the period 2015–2018. Red dots represent measurements performed immediately when the operator arrived at the flat roof (set 1) whereas green triangles represent those performed after the thermometer have adjusted to the ambient climatic conditions (set 2). Best fits considering set 1 (red line), set 2 (green line), both sets (blue line), a two-coefficient function (Equation (1), left panel) and a three-coefficient function (Equation (2), right panel) are presented.

Table 2

Coefficients of the fit equation $PW_G = a + b \bullet exp(T/c)$, determination coefficients, rms differences and percent rms differences for 3 cases: all the measurements are considered (both sets); those taken immediately when the operator arrived at the flat roof (set 1); those taken after the thermometer have adjusted to the ambient climatic conditions (set 2).

	Both sets	Set 1	Set 2
a (mm)	−3.22	−4.37	2.66
b (mm)	29.71	33.42	23.58
c (° C^{-1})	28.84	28.54	18.53
r^2	0.757	0.793	0.784
rms diff (mm)	2.95	2.68	2.82
rms diff/mean (%)	19.66	18.09	18.57

slightly higher PW_G values than those temperatures from set 2 (T_2). Tables 1 and 2 show that the regression results improve when the dataset is divided considering set 1 and set 2 separately. Furthermore, the results improve very slightly using a three-coefficient exponential fit instead of a two-coefficient one. Statistical parameters for set 1 and set 2 are similar to those of Mims et al. (2011) in their 2-year infrared thermometer study using GNSS measurements as reference and a three-coefficient exponential fit. In fact, those of set 1 using Equation (2) are even slightly better (same r^2 and lower rms diff). Note that, in comparison with the study of the above authors, our T dataset covers a longer period, our thermometer has a lower measurement threshold allowing not to miss winter measurements, our GNSS receiver is just 2 km away from the thermometer observation site (instead of 31 km), the latency of our associated GNSS measurements is 5 min (instead of 30 min), and our T dataset is filtered by discarding measurements under conditions of haze, smoke or dust in the field of view of the device. With respect to the study of Kelsey et al. (2022), who also studied the relationship between cloudless zenith sky readings by a low-cost infrared thermometer and PW, they used a two-coefficient exponential fit and obtained a rms difference of 3.64 mm (percentage rms difference and determination coefficient are not stated in their work). Due to differences in climates, we cannot use the above absolute value for a comparison. We cannot compute percentage rms difference from rms difference because the average value of the sample is not stated either. Looking at the figure of our fit (Fig. 2) we can see that our measurements comprise an approximate range of 30 mm, being approximately homogeneously distributed. By dividing the rms difference by the PW_G value of the center point of the range we can obtain an approximate value of the percentage rms difference (it is not the exact value shown in the tables of this work, but an approximation). By making this calculation with the data of the above authors (see Fig. 5 by Kelsey et al., 2022), a percentage rms difference of 23.5% is obtained. Note that the real percentage is higher because the lower half of the range contains more PW values than the upper one. One can see that this value is higher than ours considering our two-coefficient exponential fit. This higher value may be due to the fact that the above authors used as reference PW measurements from very distant radiosonde stations, i.e., weighted mean values of a station located 110 km away and 200 m higher in elevation and another 240 km away and 250 m lower with respect to the thermometer observation site, and the latency of their reference PW measurements was 12 h, whereas our reference PW_G station is 2 km away (11 m higher in elevation) and provide measurements with a 5-min latency. Note that comparing the results of Mims et al. (2011), who used a three-coefficient exponential fit, with those of Kelsey et al. (2022), who used a two-coefficient one, one may get the misleading impression that the former obtained more accurate results simply because they used a three-coefficient exponential fit. The present work (see Tables 1 and 2) demonstrate that, other factors being equal, the improvement that a three-coefficient exponential fit produces over a two-coefficient one is very slight. The key to obtaining accurate PW_t estimates is to use as reference PW measurements that are close in time to the T measurements from a station close in distance and elevation to our thermometer

observation site.

Regarding the value of the calibration coefficients, we can compare those of our three-coefficient fit with those of Mims et al. (2011) and those of our two-coefficient fit with those of Kelsey et al. (2022). Different values are observed in both comparisons. In fact, Mims et al. (2011) performed a 5-month study with several infrared thermometers and different calibration coefficients were found. Therefore, the calibration procedure must be carried out for each infrared thermometer. The different value of the calibration coefficients reflects the different spectral responses of the devices.

Unlike previous works, for the present study, two types of T measurements a day were performed, i.e., the first one immediately when the operator arrived at the flat roof carrying the thermometer (set 1) and the second one when the device had been left 1 h in the flat roof and was adjusted to the ambient climatic conditions (set 2). Tables 1 and 2 show that the regression results for set 1 are similar (even better) than those for set 2. This implies that the temperature compensation circuitry of the infrared thermometer that corrects for changes in ambient temperature works quickly and, thus, a period leaving the thermometer to adjust to the ambient climatic conditions is not necessary.

Note that, as the best results of the present study have been obtained for set 1 using Equation (2), this dataset and this equation are the ones used for the following analyses.

We now investigate whether a seasonal calibration could significantly improve the results of a normal one. Thus, calibration coefficients are obtained for each of the four seasons. Results of this analysis can be seen in Fig. 3 and Table 3. Note that, for comparison purposes, the sixth row of Table 3 contains the same data as the third column of Table 2. As expected, the lowest values of T and PW_G are in winter and the highest ones in summer. It is observed that both seasonal and total models, in general, show similar results. It must be noted that similar curves can be obtained with rather different coefficients and, therefore, it is not a surprise that coefficients can have quite different values. It is worth noting that the rms difference in the case of the full-period calibration is similar to the seasonal values, and that r^2 is better for the former probably because of the higher number of data.

Fig. 4 and Table 4 show the scatter plot and statistical values with confidence intervals of the model fit, which involves set 1, Equation (2) and full-period calibration. It can be observed that, despite the quite broad confidence intervals (we cannot forget that we are using a 20€ instrument), most of the points fall within the said intervals and the fit is quite accurate, within satellite measurement standards.

4.2. Validation

Once the calibration process is completed, a temperature reading T can be transformed into a PW_t value using the exponential function given by Equation (1) or Equation (2). As mentioned above, at this point we employ Equation (2), although both equations yield similar results. In order to check to what extent the calibration works, in the present work, a validation analysis between PW_t and PW_G is carried out using data from set 1 for the year 2019, which were not used in the calibration process.

Scatter plots between PW_G and PW_t are presented in Fig. 5 (left panel with the season-wise calibration and right panel with the full-period calibration) showing excellent agreements. Table 5 presents the intercept, slope and coefficient of determination derived from the linear regression, and, in addition, the MBE and rms difference parameters are also included in this table. These results point out that the process of calibrating an infrared thermometer with an initial set of readings and then using the equation of the best fit with subsequent readings to infer values PW_t yields good estimates. It can be seen that the values using the season-wise calibration are similar to those of the full-period calibration (they just improve slightly). Therefore, there is not a great improvement in the estimates of PW_t when the calibration is done considering seasons separately. As water vapor presents a high temporal variability (seasonal
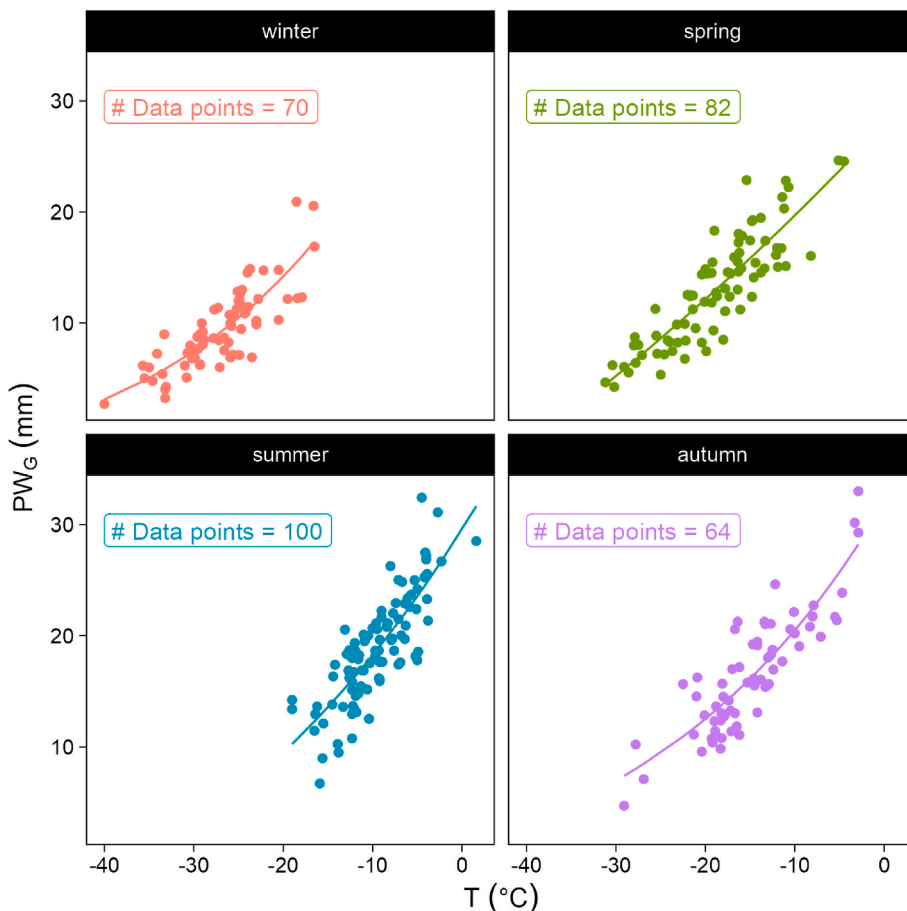
Fig. 3. Scatter plots of PW_G vs T for the period 2015–2018 and best fits with a season-wise calibration using set 1 and Equation (2). Winter includes the months December, January and February, spring the months March, April and May, summer the months June, July and August, and autumn the months September, October and November.

Table 3
Coefficients of the fit equation $PW_G = a + b \cdot exp(T/c)$ of the season-wise and full-period (total) calibrations using set 1 of data. The table also contains determination coefficients, the rms differences and the percent rms differences.

	a (mm)	b (mm)	c (°C^{-1})	r^2	rms diff (mm)	rms diff/ mean (%)
Winter	−4.80	45.50	22.90	0.688	2.02	21.21
Spring	−70.13	98.05	114.05	0.752	2.41	18.47
Summer	−20.43	49.99	38.96	0.663	2.75	14.59
Autumn	−5.54	37.52	27.37	0.754	2.64	15.81
Total	−4.37	33.42	28.54	0.793	2.68	18.09

one included), the above result indicates that GNSS and infrared thermometers track this variability similarly, which adds more value to the PW_t estimates. The result also indicates that our selection of T readings keeping only situations of clear sky without clouds, haze, smoke or dust seems to improve PW_t estimates. Said elements, which present a seasonal behavior, would have influenced T readings hampering the detection of the water vapor footprint by the infrared thermometer.

Regarding previous works, as stated in Section 1, Mims et al. (2011) did not include, compare or validate PW_t estimates in their study. Kelsey et al. (2022), who also obtained PW_t estimates from low-cost infrared thermometer measurements, compared their PW_t values with PW measurements from two stations using GNSS and sun photometer data. Note that the same T measurements that these authors used to calibrate their thermometers were then used to compute estimates, that is, they did not use an independent period of measurements to validate their estimates. They obtained rms differences of 2.43 and 2.79 and r^2 values of 0.569
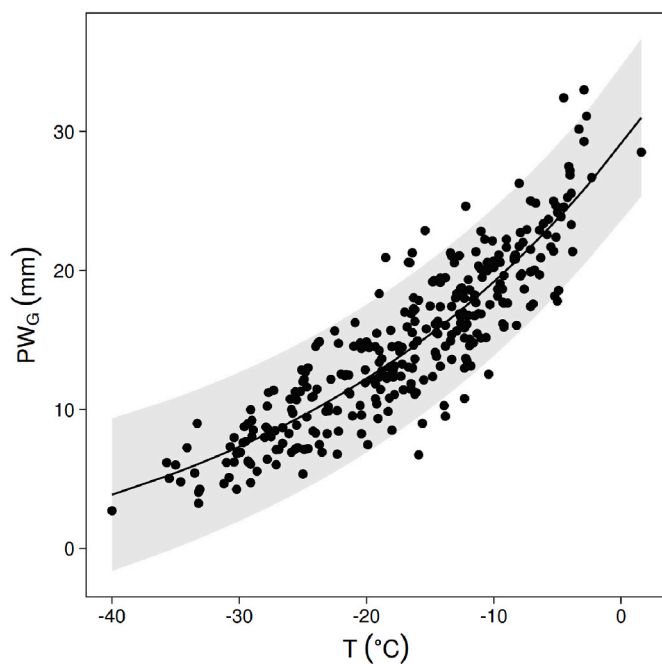

Fig. 4. Scatter plot of PW_G vs T for the period 2015–2018 for the full-period (total) calibration with set 1. The line represents the best fit considering a three-coefficient function (Equation (2)) with confidence interval as shadowed area.
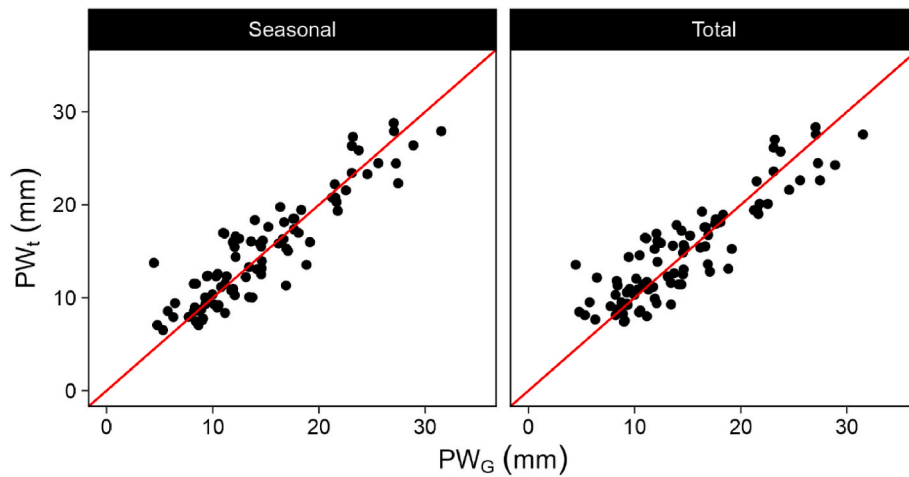
Fig. 5. Scatter plot of precipitable water derived from an infrared thermometer (PW_t) using set 1 and Equation (2) vs PW_G with data of the year 2019. Left panel contains estimates obtained from a season-wise calibration and right panel those from a full-period calibration. Red lines represent the fits of linear regressions.

Table 4
Coefficient values and their confidence interval to the 95% level of the fit equation $PW_G = a + b \cdot exp(T/c)$ of the full-period (total) calibration using the set 1 of data.

	Value	Confidence interval
a (mm)	−4.37	−15.79–0.92
b (mm)	33.42	29.10–43.60
c (°C^{-1})	28.54	20.58–46.13

Table 5
Statistics of the comparison $PW_t - PW_G$. The intercept, slope and determination coefficient are the ones of the linear regression between the two datasets. The mean bias error, rms difference and rms difference/mean are also included. The numbers in parenthesis are the uncertainties associated to these values. Second row statistics correspond to PW_t data obtained from a season-wise calibration and third row ones to those from a full-period calibration.

	Intercept (mm)	Slope	r^2	MBE (mm)	rms diff (mm)	rms diff/ mean (%)
Seasonal	0.04 (1.50)	0.97 (0.09)	0.829	0.35	2.55	17.48
Total	−0.39 (1.71)	1.01 (0.11)	0.796	0.29	2.78	19.02

and 0.624 from GNSS and sun photometer linear regression comparisons, respectively (percentage rms differences are not stated in their work). Making a calculation to infer approximate percentage rms

differences similar to that explained in subsection 4.1, values of 22.1% and 21.5% are obtained from GNSS and sun photometer, respectively (see Fig. 6 by Kelsey et al., 2022). Note that the real percentages are higher because there are many more values in the lower half of the interval than in the upper half, especially for the GNSS station. It can be checked that the validation analysis of the present work yields significantly better results (Table 5, row "total", percentage rms difference of 19.0% and r^2 of 0.796). Several factors may have contributed to the different results between works. In the stage of calibration, as mentioned in subsection 4.1, the reference PW measurements for the calibration used by the above authors came from very distant stations with large differences in altitude and in observation time with respect to the thermometer observation site and time. Regarding the stage of validation, the above authors used as reference two stations with differences in location with respect to the thermometer measurement site: the GNSS station was just 2 km away, but 750 m higher, and the sun photometer station was 30 km away (the altitude is not stated). In addition, a dry bias in comparison to radiosonde PW is documented in the sun photometer station.

In view of our results and the comparison with previous works, we can state that the key to obtaining good PW_t estimates is to have a dataset with as many T readings as possible to calibrate the thermometer and use as reference the closest PW station with similar conditions of altitude and measurement time.

It must be noted that intercomparison works of GNSS and satellite instruments for the region of the thermometer observation site (Extremadura, western Spain) yielded similar (or even worse) results
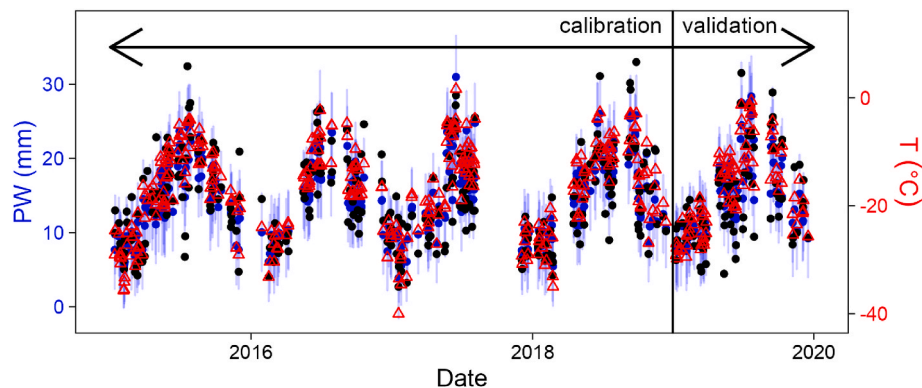

Fig. 6. Temporal evolution of T (red triangles), PW_t (blue dots) and PW_G (black dots) over the whole study period (2015–2018 calibration period, 2019 validation period). Light blue bars are the 95% confidence intervals associated with each PW_t estimate.

than those presented here. For instance, Bennouna et al. (2013) compared MODIS satellite instruments against GNSS obtaining rms differences of 20.45–23.84% and r^2 of 0.740–0.903. Román et al. (2015) validated GOME-2 against GNSS, also in this region, showing an rms difference of 31.80% and r^2 of 0.656.

Lastly, Fig. 6 displays our time series of temperature readings T, our precipitable water estimates PW_t and GNSS precipitable water measurements PW_G over the whole study period (2015–2019). From Fig. 6 we can appreciate that T can work as a proxy for PW_G since they both present similar annual variations. In addition, it can be seen that, in general, the values of the estimates from the thermometer are similar to those of the GNSS measurements. In fact, almost all the GNSS measurements are within the confidence intervals associated with each PW_t estimate. The few data points lying out of the intervals appear both below and above the intervals, and are evenly distributed over the year, thus, a significant seasonal influence is not detected. Finally, the data of the validation period show a behavior similar to that of the data of the calibration period. Therefore, again, the results confirm that the infrared thermometer produces good estimates of precipitable water.

4.3. Dependence analysis

This subsection studies the influence of the precipitable water content and solar zenith angle (SZA) on rms differences. This is achieved by grouping data of similar PW_t or SZA into bins and calculating the rms difference for each bin. Fig. 7 exhibits rms differences on bins of 2 mm of PW_t. Only representative bins (more than 5 data) are shown. The results among the datasets are comparable (~3 mm), with rather stable values. Precipitable water content dependence does not present a clear pattern. Values typically change in the 2–4 mm range. Two local maxima appear around 12–14 mm and 22 mm with minima at the extremes of the interval and at 18 mm.

SZA dependence is studied using bins of 2°. The rms differences for each SZA bin are represented in Fig. 8. Again, only representative bins (more than 5 data) are shown. The general behavior is to decrease rms differences as SZA increases. The reason for this behavior may be that direct sunlight reaching the thermometer sensor can induce noise in the
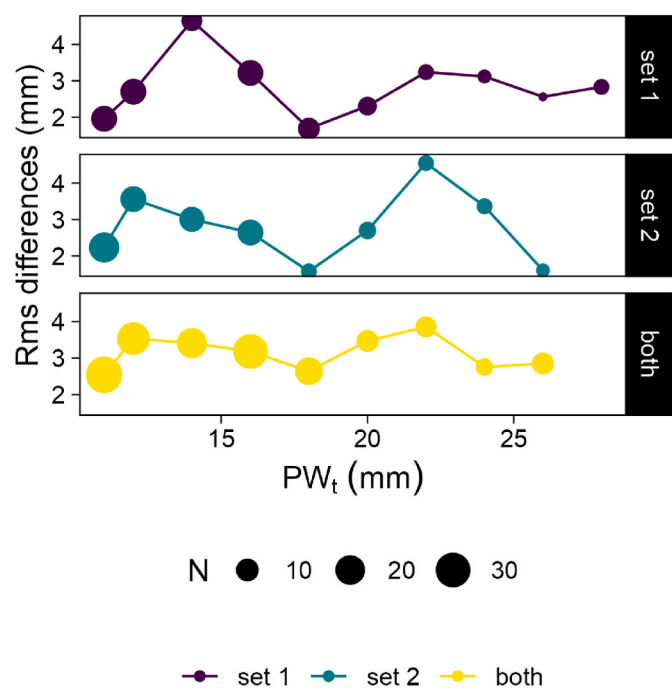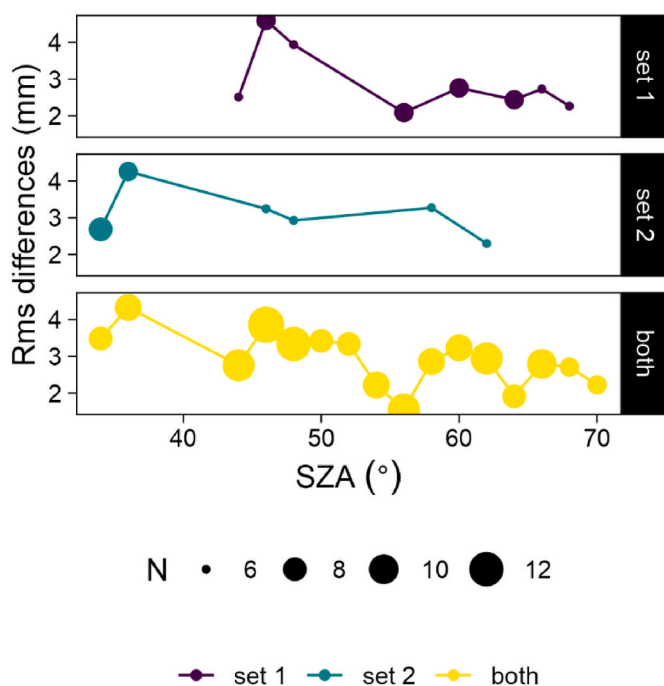

Fig. 8. Rms differences of different solar zenith angle (SZA) bins (2° width) with set 1 (top panel), set 2 (middle panel) and both sets (bottom panel). The size of the points indicate the number of data.

measurements. As the thermometer must be pointed at the zenith, the smaller the SZA the easier direct sunlight can enter the thermometer sensor. This effect could explain why the set 1 of T measurements produces slightly better results than the set 2 (set 1 includes measurements taken 1 h earlier than those of the set 2, both before midday, thus involving larger SZA).

5. Conclusions

The present work compares daily measurements (T) taken by a low-cost infrared thermometer pointed at the cloudless zenith sky in Badajoz (Spain) for 5 years with precipitable water vapor measurements recorded by a nearby GNSS station (PW_G). Through regression analyses for the data period 2015–2018 (calibration period) equations of exponential fits are obtained. These equations together with thermometer readings for the year 2019 as input yield PW estimates (PW_t), which are compared with PW_G measurements in a validation analysis. This analysis proves that the thermometer yields PW_t estimates with rms differences of 19% when the calibration was performed in a normal way, i.e., considering one equation, and 17% when the calibration was performed seasonally, i.e., one equation per season. These estimates are of an accuracy similar (or even better) to that of satellite measurements.

Our results, when compared with those of previous works, indicate that, in order to obtain good estimates, it is important to have a sufficient number of thermometer readings and to use PW measurements close in time to the T readings from a nearby station with a similar elevation as reference for the calibration. We have also demonstrated that the use of a three-coefficient exponential equation to convert T readings into PW_t estimates produces hardly any improvement with respect to the use of a two-coefficient one. In contrast, a dependence analysis have shown that solar elevation affects the quality of the estimates. This highlights the importance of keeping the thermometer field of view as far away from direct solar radiation as possible.

We hope that this study will contribute to encourage people to create a dense network that improves the spatial and temporal variability of water vapor. Even students and non-expert weather observers can employ the procedure tested in the present work. They only need an

Fig. 7. Rms differences of different PW_t bins (2 mm width) with set 1 (top panel), set 2 (middle panel) and both sets (bottom panel). The size of the points indicate the number of data.

inexpensive infrared thermometer, PW measurements from a nearby station (the website we provide in this work contains GNSS data from stations around the world), and a basic knowledge of a simple software, e.g., a spreadsheet, to calculate de calibration coefficients of their infrared thermometer.

Author contributions

Conceptualization, A.J.P.A., J.V.-M., M.C.G., M.A. and J.M.V.; methodology, A.J.P.A., J.V.-M., M.C.G., M.A. and J.M.V.; software, A.J.P.A. and J.V.-M.; validation, A.J.P.A., J.V.-M., M.C.G., M.A. and J.M.V.; formal analysis, A.J.P.A. and J.V.-M.; investigation, A.J.P.A.; resources, J.M.V.; data curation, A.J.P.A. and J.V.-M.; writing-original draft preparation, A.J.P.A. and J.V.-M.; writing-review and editing, A.J.P.A., J.V.-M., M.C.G., M.A. and J.M.V.; visualization, A.J.P.A. and J.V.-M.; supervision, M.C.G., M.A. and J.M.V.; project administration, M.C.G., M.A. and J.M.V.; funding acquisition, M.C.G. and J.M.V. All authors have read and agreed to the published version of the manuscript.

Funding

Declaration of competing interest

The authors declare that they have no known competing financial interests or personal relationships that could have appeared to influence the work reported in this paper.

Data availability

Data will be made available on request.

References

Bennouna, Y.S., Torres, B., Cachorro, V.E., Ortiz de Galisteo, J.P., Toledano, C., 2013. The evaluation of the integrated water vapour annual cycle over the Iberian Peninsula from EOS-MODIS against different ground-based techniques. Q. J. R. Meteorol. Soc. 139, 1935–1956. https://doi.org/10.1002/qj.2080.

Bevis, M., Businger, S., Chiswell, S., Herring, T.A., Anthes, R.A., Rocken, C., Ware, R.H., 1994. GPS meteorology: mapping zenith wet delays onto precipitable water. J. Appl. Meteorol. 33, 379–386. https://doi.org/10.1175/1520-0450(1994)033<0379:GMMZWD>2.0.CO;2.

Bevis, M., Businger, S., Herring, T.A., Rocken, C., Anthes, R.A., Ware, R.H., 1992. GPS meteorology: remote sensing of atmospheric water vapor using the global positioning system. J. Geophys. Res. 97, 15787 https://doi.org/10.1029/92JD01517.

Blewitt, G., Hammond, W., Kreemer, C., 2018. Harnessing the GPS Data Explosion for Interdisciplinary Science, 99. Eos, Washington. DC. https://doi.org/10.1029/2018EO104623.

Bokoye, A.I., Royer, A., O'neill, N.T., Cliche, P., Mcarthur, L.J.B., Teillet, P.M., Fedosejevs, G., Thériault, J.-M., 2003. Multisensor analysis of integrated atmospheric water vapor over Canada and Alaska. J. Geophys. Res. 108, 4480. https://doi.org/10.1029/2002JD002721.

Buehler, S.A., Östman, S., Melsheimer, C., Holl, G., Eliasson, S., John, V.O., Blumenstock, T., Hase, F., Elgered, G., Raffalski, U., Nasuno, T., Satoh, M., Milz, M., Mendrok, J., 2012. A multi-instrument comparison of integrated water vapour measurements at a high latitude site. Atmos. Chem. Phys. 12, 10925–10943. https://doi.org/10.5194/acp-12-10925-2012.

Colman, R., 2003. A comparison of climate feedbacks in general circulation models. Clim. Dynam. 20, 865–873. https://doi.org/10.1007/s00382-003-0310-z.

Colman, R.A., 2015. Climate radiative feedbacks and adjustments at the Earth's surface. J. Geophys. Res. Atmos. 120, 3173–3182. https://doi.org/10.1002/2014JD022896.

Guerova, G., Jones, J., Douša, J., Dick, G., de Haan, S., Pottiaux, E., Bock, O., Pacione, R., Elgered, G., Vedel, H., Bender, M., 2016. Review of the state of the art and future prospects of the ground-based GNSS meteorology in Europe. Atmos. Meas. Tech. 9, 5385–5406. https://doi.org/10.5194/amt-9-5385-2016.

Idso, S.B., 1982. Humidity measurement by infrared thermometry. Remote Sens. Environ. 12, 87–91. https://doi.org/10.1016/0034-4257(82)90009-8.

Kelsey, V., Riley, S., Minschwaner, K., 2022. Atmospheric precipitable water vapor and its correlation with clear-sky infrared temperature observations. Atmos. Meas. Tech. 15, 1563–1576. https://doi.org/10.5194/amt-15-1563-2022.

Mims III, F.M., Chambers, L.H., Brooks, D.R., 2011. Measuring total column water vapor by pointing an infrared thermometer at the sky. Bull. Am. Meteorol. Soc. 92, 1311–1320. https://doi.org/10.1175/2011BAMS3215.1.

Morris, V.R., Long, C.N., Nelson, D., 2006. Deployment of an infrared thermometer network at the atmospheric radiation measurement program southern great plains climate research facility. In: 16th ARM Science Team Meeting. U.S. Dept. Energy, Albuquerque, NM, pp. 1–11.

Myhre, G., Shindell, D., Br'eon, F.-M., Collins, W., Fuglestvedt, J., Huang, J., Koch, D., Lamarque, J.-F., Lee, D., Mendoza, B., Nakajima, T., Robock, A., Stephens, G., Takemura, T., Zhang, H., 2013. Anthropogenic and natural radiative forcing. In: Climate Change 2013: the Physical Science Basis. Contribution of Working Group I to the Fifth Assessment Report of the Intergovernmental Panel on Climate Change. IPCC, pp. 659–740.

Negusini, M., Petkov, B.H., Tornatore, V., Barindelli, S., Martelli, L., Sarti, P., Tomasi, C., 2021. Water vapour assessment using GNSS and radiosondes over polar regions and estimation of climatological trends from long-term time series analysis. Rem. Sens. 13, 4871. https://doi.org/10.3390/rs13234871.

Román, R., Antón, M., Cachorro, V.E., Loyola, D., Ortiz de Galisteo, J.P., de Frutos, A., Romero-Campos, P.M., 2015. Comparison of total water vapor column from GOME-2 on MetOp-A against ground-based GPS measurements at the Iberian Peninsula. Sci. Total Environ. 533, 317–328. https://doi.org/10.1016/j.scitotenv.2015.06.124.

Vaquero-Martínez, J., Antón, M., 2021. Review on the role of GNSS meteorology in monitoring water vapor for atmospheric physics. Rem. Sens. 13, 2287. https://doi.org/10.3390/rs13122287.

Vaquero-Martínez, J., Antón, M., Ortiz de Galisteo, J.P., Román, R., Cachorro, V.E., Mateos, D., 2019. Comparison of integrated water vapor from GNSS and radiosounding at four GRUAN stations. Sci. Total Environ. 648, 1639–1648. https://doi.org/10.1016/j.scitotenv.2018.08.192.